https://doi.org/10.5194/essd-2025-695
Preprint. Discussion started: 20 January 2026


Open Access Earth System Science Data Discussions

# Decadal surge of water-surface solar in China's Yangtze Delta: A high-fidelity SAR-optical fusion inventory (2015–2024)

Yue Yan[1], Xin Jiang[1,*], Sihuan Wei[2,3,4], Yubin Jin[2,5], Xinyu Zou[1], Junwei Liu[4], Yaotong Cai[1], Jianhuai Ye[1], Zhilin Guo[1], Zhenzhong Zeng[1,*]

[1] School of Environmental Science and Engineering, Southern University of Science and Technology, Shenzhen 518055, China

[2] Zhejiang Key Laboratory of Industrial Intelligence and Digital Twin, Eastern Institute of Technology, Ningbo, Zhejiang, P.R. China

[3] Department of Building Environment and Energy Engineering, The Hong Kong Polytechnic University, Kowloon, Hong Kong, China

[4] Internatiaonl Centre of Urban Energy Nexus, The Hong Kong Polytechnic University, Kowloon, Hong Kong, China

[5] Department of Computing, The Hong Kong Polytechnic University, Hong Kong, China

[*] *Correspondence to*: Zhenzhong Zeng (zengzz@sustech.edu) and Xin Jiang (jiangx@sustech.edu.cn)

Manuscript for *Earth System Science Data*

November 18, 2025

https://doi.org/10.5194/essd-2025-695
Preprint. Discussion started: 20 January 2026


Open Access Earth System Science Data Discussions

**Abstract:** China hosts approximately 97% of the world's water-surface photovoltaics (WPV), with nearly two-thirds of its national capacity concentrated in the Yangtze River Delta (YRD), a densely populated economic powerhouse facing intense land-energy trade-offs. Despite this dominance, no high-resolution, decade-long inventory has existed to track this rapid expansion. WPV detection using optical RS imagery is severely limited by persistent cloud cover, water surface reflections, and spectral confusion, compromising long-term consistency over aquatic environments. Here, we developed a multi-sensor fusion framework integrating all-weather Sentinel-1 Synthetic Aperture Radar (SAR) and annual composite Sentinel-2 optical imagery. Key features include six Sentinel-2 bands, spectral indices (NDVI, MNDWI, NDBI, NDPI, and SAVI), texture metrics, and dual-polarization SAR backscatter. We trained a Random Forest classifier on 55,849 verified samples to generate annual WPV maps for 2015-2024. Afterwards, we applied post-processing procedures, including noise removal, patch merging, and area thresholding, and further validated installation years and eliminated errors through manual inspection of Google Earth time-series imagery. The well-constructed dataset of the first 10 m-resolution WPV atlas for the YRD maps 401 validated projects with a cumulative area of 145.4 $km^2$ by 2024. It outperforms existing global PV inventories with an overall accuracy of 97.3% and a Kappa coefficient of 0.94. The results reveal rapid expansion from 17.4 $km^2$ in 2015 to 145.4 $km^2$ in 2024, with 87% deployed on natural lakes, with a marked shift in leadership from Jiangsu to Anhui, and clear spatial clustering near grid infrastructure and stable water bodies. This high-fidelity inventory provides a robust foundation for monitoring WPV evolution, assessing environmental impacts, and informing sustainable energy planning in the world's leading floating solar region.

**Keywords:** Water-surface photovoltaics, Yangtze River Delta, Sentinel-1/2 fusion, Time-series mapping, Random Forest classification

https://doi.org/10.5194/essd-2025-695
Preprint. Discussion started: 20 January 2026




## 1 Introduction

The global shift from carbon-intensive energy systems to carbon-extensive renewables is accelerating in response to growing electricity demand and the urgent need to mitigate climate change. Solar photovoltaics (PV) dominates its growth, owing to its continued cost declines, and accounted for nearly 80% of new capacity additions in 2024 (Anon, 2025; Bogdanov *et al.*, 2021). However, the substantial land footprint required by conventional PV systems increasingly conflicts with agriculture and other critical land uses (Capellán-Pérez *et al.*, 2017; van de Ven *et al.*, 2021; Wei *et al.*, 2025). Water-surface photovoltaics (WPV) emerges as a promising alternative. Deployed on natural lakes, reservoirs, and other water bodies, WPV alleviates land-use competition while offering additional benefits, such as reduced water evaporation loss (Forester *et al.*, 2025; Pouran *et al.*, 2022; Jin *et al.*, 2023). China hosts approximately 97% of global WPV, with nearly two-thirds of its national capacity concentrated in the water-abundant, energy-intensive Yangtze River Delta (YRD) region (Chen *et al.*, 2024). For the YRD and similar regions, understanding the spatial dynamics and scalability of WPV is crucial for optimizing renewable energy strategies that balance energy security, land stewardship, and ecosystem sustainability.

In recent years, remote sensing combined with machine learning has become prevalent for extracting photovoltaic installations at regional or global scales (Zhang *et al.*, 2023; Ortiz *et al.*, 2022; Zhang *et al.*, 2022). Among these, classification algorithms such as Random Forest have demonstrated strong performance and robustness (Belgiu and Drăguţ, 2016). These techniques typically leveraged spectral, geometric, and textural features from satellite imagery to enable efficient, large-scale PV detection (Zhang *et al.*, 2021; Chen *et al.*, 2022). Despite these advances, several challenges persist, particularly for complex aquatic environments and long-term monitoring. Optical imagery, which forms the foundation of most existing methods, is highly sensitive to weather conditions such as clouds, fog, and overcast skies, and cannot acquire data at night. Over water bodies, its performance is further constrained by reflections and shadows. Furthermore, although per-image accuracies can exceed 96% (Kruitwagen *et al.*, 2021; Xia *et al.*, 2022, 2023), small errors accumulate substantially in long-term time-series

https://doi.org/10.5194/essd-2025-695
Preprint. Discussion started: 20 January 2026




mapping. For instance, mapping with 96% annual accuracy over a decade yields only about 67% consistency across the full period ($0.96^{10} \approx 0.67$). This compounded uncertainty, effectively rendering one-third of time-series outcomes unreliable, complicates spatiotemporal assessments and often results in confusion between photovoltaic installations and water surfaces. As a result, ensuring both temporal consistency and high fidelity in long-term water-based PV mapping remains a key methodological challenge.

To directly address these limitations, this study proposes a robust and multidimensional feature-fusion framework for WPV extraction in the YRD region. Our approach utilizes annual composite Sentinel-2 imagery (2015-2024) and incorporates Sentinel-1 SAR observations to provide all-weather detection and capture strong backscatter signatures of WPV's metallic structures. This combination substantially enhances single-period mapping accuracy and reduces misclassifications. To ensure comprehensive spatial coverage, we first identified candidate WPV zones through multi-year temporal compositing and water-mask filtering, thereby constraining detection to likely water-based locations and suppressing non-water interference. Subsequently, all detected WPV regions underwent rigorous manual inspection and refinement using high-resolution Google Earth imagery. This step enabled the precise removal of false positives and the reliable determination of installation years. The resulting decade-long WPV dataset achieves unprecedented accuracy and temporal consistency, representing the most reliable long-term inventory of WPV development to date and providing a robust foundation for understanding spatiotemporal growth dynamics and policy-relevant deployment patterns.

## 2 Datasets and Methods

### 2.1 Study Area

China leads the world in WPV system development, holding approximately 96.82% of the global WPV-installed surface area in 2019, as shown in Fig. 1a. Within China, the YRD region represents a significant WPV hub, accounting for nearly two-thirds of the national total.

https://doi.org/10.5194/essd-2025-695
Preprint. Discussion started: 20 January 2026




Specifically, Jiangsu (30.21%), Anhui (19.75%), and Zhejiang (9.97%) provinces exhibit the highest installed WPV capacities (Xia *et al.*, 2022, 2023).

Located in eastern China along the lower reaches of the Yangtze River (Fig. 1b), the YRD is characterized by abundant water resources, including a dense network of rivers, lakes, and reservoirs (Fig. 1c). These natural conditions are highly favorable for large-scale WPV deployment. Moreover, as one of China's most economically developed and industrially concentrated areas, the YRD faces substantial electricity demand (Xu *et al.*, 2023). The rapid growth of WPV in this region not only helps alleviate regional energy pressures but also plays a vital role in energy restructuring and the transition toward low-carbon development. Considering its current deployment scale, water resource conditions, and future development potential, this study focuses on the YRD as its primary research area.

## 2.2 Datasets

### 2.2.1 Satellite Datasets

This study primarily utilizes Sentinel-1 Synthetic Aperture Radar (SAR) and Sentinel-2 Multispectral Instrument (MSI) imagery, both of which are accessible via the Google Earth Engine (GEE) platform. The selected temporal coverage, from 2015 to 2024, aligns with the rapid development timeline of WPV installations in China.

Sentinel-1, equipped with a C-band SAR sensor, provides all-weather, day-and-night imaging capabilities, making it ideal for long-term dynamic monitoring as it's unaffected by cloud cover, precipitation, or illumination. We utilized the Sentinel-1 Ground Range Detected product from GEE, which features a 10-meter spatial resolution and a 6–12-day revisit time. To comprehensively capture radar backscatter characteristics of water bodies and WPV structures, Vertical Transmit/Vertical Receive (VV) and Vertical Transmit/Horizontal Receive (VH) polarization channels were selected.

Sentinel-2 provides high-resolution, multispectral optical and near-infrared imagery, well-suited for identifying and classifying WPV regions. We utilized atmospherically corrected

https://doi.org/10.5194/essd-2025-695
Preprint. Discussion started: 20 January 2026




Level-2A surface reflectance products from the Sentinel-2 MSI sensor, which provides 13 spectral bands. Six key bands sensitive to water bodies and artificial structures were selected: Bands 2–4 (visible), Band 8 (NIR), and Bands 11–12 (SWIR), all at 10-meter resolution with a 5-day revisit. To reduce cloud interference, a cloud-masking algorithm was applied, and annual median composites were generated from all available images (Gorelick *et al.*, 2017). To reduce cloud interference, a cloud-masking algorithm was applied, and annual median composites were generated from all available images. These composites ensure radiometric consistency and provide a stable spatial baseline for dynamic WPV detection and temporal analysis. These composites ensure radiometric consistency and provide a stable spatial baseline for dynamic WPV detection and temporal analysis.

### 2.2.2 Water Body Datasets

A water mask of the Yangtze River Delta (YRD) was constructed to geographically delineate the study area. It was based on several publicly available global water and reservoir datasets, including HydroLAKES, GRanD, GOODD, and GeoDar (Lehner *et al.*, 2011; Messager *et al.*, 2016; Mulligan *et al.*, 2020; Wang *et al.*, 2022). The HydroLAKES dataset provides spatial boundaries and multiple attributes (e.g., area, storage capacity, and mean depth) of global natural lakes and some artificial lakes, enabling the identification of small lakes and potential host water bodies for floating photovoltaics. The GRanD dataset records the locations, capacities, construction years, and purposes of large reservoirs and dams worldwide, facilitating the identification of artificial reservoirs. GOODD and GeoDar provide georeferenced dam locations derived from remote sensing, which further complement GRanD and enable high-precision spatial mapping of reservoirs and dams.

In the data processing procedure, natural lakes were defined as all water bodies excluding artificial reservoirs, encompassing aquaculture ponds and irrigation ponds. By integrating these four datasets, a foundational water layer for the study area was generated. This layer provides a stable spatial reference and serves as a validation framework for identifying water-surface photovoltaics using Sentinel-1 SAR and Sentinel-2 optical imagery.

https://doi.org/10.5194/essd-2025-695
Preprint. Discussion started: 20 January 2026




155

156 **2.2.3 Training and Validation Samples**

157 The training and validation samples used in this study were derived from the WPV
158 inventory (Xia *et al.*, 2022), which mapped the distribution of WPV installations in China for
159 2021. Because the original dataset contained several misclassified regions, a manual
160 verification process was conducted to ensure the reliability of the labels. Each WPV polygon
161 was visually checked using high-resolution satellite imagery, and misidentified areas were
162 removed. WPV sample points were generated proportionally to the area of each PV polygon to
163 ensure adequate representation of large installations. Examples from three representative WPV
164 regions are shown in Figs. 2a–c, demonstrating typical distribution patterns across different
165 water bodies. Non-WPV samples were randomly selected from water surfaces without PV
166 coverage to provide balanced class representation.

167 The spatial distribution of all sample points is illustrated in Fig. 2d, where red points
168 represent WPV samples and blue points represent non-PV samples. In total, the dataset consists
169 of 55,849 labeled points (80% for training and 20% for validation), including 28,332 WPV and
170 27,517 non-WPV samples (Fig. 2e). These well-validated samples formed the foundation for
171 subsequent annual classifications from 2015 to 2024.

172

173 **2.3 WPV Extraction Workflow**

174 **2.3.1 WPV Feature Engineering**

175 To reduce data volume and focus on aquatic areas, we first filtered Sentinel-2 MSI imagery
176 using a water mask, effectively excluding most terrestrial regions. Six spectral bands (Bands 2–
177 4 [visible], Band 8 [NIR], and Bands 11–12 [SWIR]) were selected as key features due to their
178 sensitivity to water bodies and artificial structures. To minimize the influence of cloud cover
179 and provide stable annual surface conditions, annual median composites were generated from
180 all available images within each year. To enhance the distinction between water bodies and
181 WPV installations, we integrated a comprehensive set of additional features:

https://doi.org/10.5194/essd-2025-695
Preprint. Discussion started: 20 January 2026




**Spectral indices:** Normalized Difference Vegetation Index (NDVI), Modified Normalized Difference Water Index (MNDWI), Normalized Difference Built-up Index (NDBI), Normalized Difference Photovoltaic Index (NDPI), and Soil-Adjusted Vegetation Index (SAVI), based on Eqs. (1)–(5). These indices have proven effective in photovoltaic detection (Feng *et al.*, 2024), with NDVI and MNDWI aiding in the identification of water bodies, NDBI and NDPI improving the discrimination of WPV, and SAVI reducing interference from vegetation/soil.

$$NDVI = \frac{\rho(NIR) + \rho(RED)}{\rho(NIR) - \rho(RED)} \quad (1)$$

$$MNDWI = \frac{\rho(GREEN) + \rho(MIR)}{\rho(GREEN) - \rho(MIR)} \quad (2)$$

$$NDBI = \frac{\rho(SWIR1) + \rho(NIR)}{\rho(SWIR1) - \rho(NIR)} \quad (3)$$

$$NDPI = \frac{\rho(NIR) - \rho(SWIR2)}{\rho(SWIR1) - \rho(NIR)} \quad (4)$$

$$SAVI = 1.5\frac{\rho(NIR) - \rho(RED)}{\rho(NIR) + \rho(RED) + 0.5} \quad (5)$$

**Texture features:** Computed using the Gray Level Co-occurrence Matrix (Haralick *et al.*, 1973), these features capture the distinct spatial patterns of WPV arrays, which typically exhibit clear, regular boundaries contrasting with natural water bodies.

**SAR-based backscatter data:** We incorporated annual mean values from Sentinel-1 SAR VV and VH polarization bands to provide complementary all-weather backscatter information, crucial for robust WPV identification, especially over water.

### 2.3.2 Annual WPV Classification

Classification was conducted using the Random Forest algorithm implemented within the Google Earth Engine (GEE) platform, selected for its robustness, computational efficiency, and demonstrated success in PV mapping tasks (Feng *et al.*, 2024; Zhang *et al.*, 2023). The Random Forest classifier was trained on a labeled sample dataset derived from both WPV and non-WPV-covered water bodies (Fig. 3a). After model training, the classifier was applied to annual

https://doi.org/10.5194/essd-2025-695
Preprint. Discussion started: 20 January 2026


imagery to perform classification for each year from 2015 to 2024, producing a decade-long time series of WPV distribution maps.

### 2.3.3 Automated Post-Processing

Following the initial classification, we applied a systematic post-processing methodology to refine the results, remove non-WPV areas, and consolidate adjacent patches. This process, consistent with previous work (Hirayama *et al.*, 2019), aimed to improve overall map quality and reduce the workload for subsequent visual interpretation (Fig. 3b). Given that WPV installations typically occupy relatively large areas, we first performed noise removal by identifying and eliminating classified patches with fewer than 10 pixels. Additionally, WPV arrays located in close proximity within the same water body are often part of the same project and installed concurrently. To accurately represent this, adjacent patches within a 100-meter buffer (i.e., less than 200 meters apart) were merged into single units. Finally, recognizing that larger WPV patches generally correlate with higher classification accuracy, only those with an area greater than 0.001 $km^2$ were retained in the final results, ensuring the inclusion of reliable WPV installations.

## 2.4 Accuracy Assessment and Manual Refinement

### 2.4.1 Classification Model Assessment

To support the classification workflow, a stratified random sample comprising 20% of the total dataset (5,667 WPV points and 5,507 non-WPV) was held out for independent accuracy assessment. Classification performance was evaluated using four standard metrics: User Accuracy (UA), Producer Accuracy (PA), Overall Accuracy (OA), and the Kappa coefficient.

### 2.4.2 Manual Refinement and Final Dataset Creation

To achieve the highest accuracy and completeness in our WPV extraction, we integrated

https://doi.org/10.5194/essd-2025-695
Preprint. Discussion started: 20 January 2026




the annual classified WPV maps (2015–2024) with external WPV datasets (Xia *et al.*, 2022), creating a comprehensive set of potential WPV regions. Each potential region was then subjected to rigorous manual interpretation and correction using high-resolution satellite imagery from Google Earth (Fig. 3c). This critical validation step enabled the precise identification and removal of misclassified non-WPV areas, thereby significantly enhancing the reliability of our final dataset. As WPV installations are typically long-lasting, their installation year was accurately estimated by identifying the first year each site visibly appeared in high-resolution Google Earth imagery sequences. This approach allowed for a more systematic and accurate understanding of WPV deployment over time. Finally, internal gaps within the identified WPV patches were filled to ensure spatial completeness, facilitating more precise calculations of area and surface coverage.

## 3 Result

### 3.1 Accuracy Validation and Comparison of WPV Extraction Results

To comprehensively evaluate the reliability and robustness of our WPV extraction results, we conducted a multi-level validation and comparison process. This section presents a systematic assessment of the classification performance from three complementary perspectives. First, the initial classification outputs were visually inspected and refined to evaluate the effectiveness of the post-processing procedure. Then, single-year and multi-year merged datasets were compared to examine the temporal stability of WPV detection results. Finally, our dataset was compared with existing global PV products, including a global inventory of photovoltaic solar energy generating units as of the end of 2018 (Kruitwagen et al., 2021) and Global Renewables Watch in 2024 (Robinson *et al.*, 2025), to assess spatial completeness and consistency. Both qualitative and quantitative analyses were performed, including confusion-matrix-based accuracy assessment and detailed visual interpretation across representative regions. Together, these evaluations provide a thorough verification of the accuracy, continuity, and advantages of our WPV dataset.

https://doi.org/10.5194/essd-2025-695
Preprint. Discussion started: 20 January 2026




259

260 **3.1.1 Evaluation of Initial and Refined WPV Extraction Results**

261 To visually assess the effectiveness of our post-processing workflow, we compared the
262 initial and refined WPV classification results (Fig. 4). The initial classification results (Figs. 4b,
263 e, h) contained a certain level of noise and misclassification, including small isolated patches
264 and fragmented boundaries along water edges. These inaccuracies were mainly caused by
265 spectral confusion between WPV installations and nearby structures or floating vegetation.
266 After systematic post-processing and manual correction (Figs. 4c, f, i), the final results exhibited
267 much cleaner boundaries and more coherent WPV patches. The red outlines clearly delineate
268 WPV areas, demonstrating improved spatial consistency and a reduction in false positives. This
269 refinement process substantially enhanced the reliability of the extracted WPV maps, providing
270 a foundation for subsequent accuracy validation and spatial analysis.

271

272 **3.1.2 Comparison Between Single-Year and Multi-Year Merged Results**

273 We compare WPV extraction results obtained from single-year imagery with those derived
274 from merged multi-year datasets (Figs. 5, 6), providing an assessment of the benefits of
275 temporal data integration. The results indicate that single-year classifications on both lakes and
276 reservoirs frequently suffered from incomplete coverage (Figs. 5a–b, d–e, g–h and 6a–b, d–e,
277 g–h), resulting in fragmented or missing WPV patches due to cloud contamination or partial
278 image coverage. By contrast, the merged 2015–2024 dataset (Figs. 5c, f, i and 6c, f, i) offered
279 a more consistent and complete delineation of WPV boundaries, as highlighted by the orange
280 outlines. These improvements are particularly notable in turbid or seasonally fluctuating water
281 bodies, where single-year imagery alone may fail to capture stable WPV features. Overall, the
282 multi-year merging strategy substantially enhanced both classification completeness and spatial
283 continuity, providing a robust basis for temporal analyses of WPV expansion.

284

https://doi.org/10.5194/essd-2025-695
Preprint. Discussion started: 20 January 2026




#### 3.1.3 Comparison with Existing Global PV Datasets

We compared our WPV dataset with a global inventory of photovoltaic solar energy-generating units and Global Renewables Watch in terms of statistical accuracy. Six representative locations were selected to assess the performance of our dataset relative to these global datasets (Figs. 7, 8). Visual inspection indicates that the existing global datasets exhibit notable limitations in WPV identification, frequently resulting in misclassification or omission, particularly in small-scale or spatially complex inland water bodies. Fig. 7 highlights instances of incomplete or erroneous WPV identification, whereas Fig. 8 shows multiple WPV regions that were entirely missed by the global datasets but were successfully captured in our study.

Quantitative accuracy assessment (Table 1) further confirms the superior performance of our dataset. Specifically, our WPV dataset achieved an Overall Accuracy (OA) and Kappa coefficient exceeding 0.9, while the corresponding metrics for the two global datasets were generally lower (OA: 0.825–0.818, Kappa: 0.651–0.637). These results demonstrate that our dataset significantly outperforms existing global datasets in terms of both classification accuracy and spatial completeness, validating that the integration of multi-temporal imagery with regionally representative sample training can substantially enhance the accuracy and reliability of WPV extraction.

### 3.2 WPV Spatiotemporal Distribution and Growth Trends

WPV projects in the study area exhibit distinct spatiotemporal distribution and growth trends. Spatially, current WPV projects are primarily concentrated in Anhui and Jiangsu provinces, which provide suitable hydrological and land-use conditions for large-scale deployment (Fig. 9a). By 2024, a total of 401 WPV projects have been identified in the YRD, covering a cumulative area of 145.5 $km^2$. Among these, Anhui Province hosts the largest share (68.7 $km^2$), accounting for 47% of the total WPV area, followed by Jiangsu (64.8 $km^2$) and Zhejiang (12 $km^2$). Based on the five largest WPV projects in each province (Table 2), Jiangsu generally exhibits a larger overall project scale, with most large WPV installations located on

https://doi.org/10.5194/essd-2025-695
Preprint. Discussion started: 20 January 2026


lakes.

From a temporal perspective, WPV installations have expanded markedly between 2015 and 2024, with the total area increasing by 128 $km^2$ (Fig. 9b). This expansion was most pronounced during the early phase (2015–2019), which contributed approximately 59.2% of the total increase, followed by a relative slowdown during 2019–2024. At the provincial level, Anhui experienced the greatest increase in WPV area over the decade, adding 66.9 $km^2$, followed by Jiangsu (49.1 $km^2$), while Zhejiang's growth remained modest, with a total addition of only 12 $km^2$. Notably, the spatial evolution trajectories of WPV deployment differ significantly among the three provinces. In Jiangsu, WPV development began in the northern region and gradually expanded southward and toward the coastal areas during the early years. In contrast, early WPV projects in Anhui were also concentrated in the north, but from 2022 onward, installations rapidly expanded along the Yangtze River corridor, forming a more continuous, belt-shaped distribution. Zhejiang Province, by comparison, saw only limited WPV deployment, characterized by a short burst of growth between 2017 and 2020, with most projects clustered in its northern and western regions.

In addition to the overall spatial and temporal patterns in the YRD, WPV projects of different sizes exhibit distinct trends in quantity and growth, providing additional insights into the structural characteristics of PV development in the region(Fig. 9b). Large-scale projects (> 1.0 $km^2$) are relatively few, experiencing rapid growth primarily between 2015 and 2018, then stabilizing. Conversely, medium-scale (0.1–1.0 $km^2$) and small-scale (<0.1 $km^2$) projects far outnumber large ones and have grown rapidly overall. In general, WPV development has evolved from localized concentrations to broader regional deployment, and from predominantly large-scale projects to a more diversified mix of small-scale and medium-scale systems.

### 3.3 WPV Deployment on Lakes and Reservoirs

Different types of water bodies exhibit varying levels of adaptability to WPV deployment, which directly affects the estimation of potential installed capacity and informs rational spatial

https://doi.org/10.5194/essd-2025-695
Preprint. Discussion started: 20 January 2026




planning(Bai *et al.*, 2024; Château *et al.*, 2019). Within the study area, WPV installations are predominantly located on lakes, with only a minor proportion situated on reservoirs (Fig. 10a). Lakes host the vast majority of total capacity—exceeding 126.8 $km^2$ by 2024, or 87.2% of the cumulative WPV area. In contrast, reservoirs account for 12.8% (18.6 $km^2$) of total WPV deployment. However, the distribution across waterbody types differs considerably among provinces. Jiangsu exhibits the most pronounced disparity, with approximately 98.1% of its WPV systems deployed on lakes and only 1.9% on reservoirs. Anhui and Zhejiang demonstrate higher shares of reservoir-based WPV, at 28.9% and 20.2%, respectively. The temporal evolution of WPV deployment also reveals distinct trajectories for lakes and reservoirs (Fig. 10b). Lake-based WPV installations expanded steadily between 2015 and 2024, with a total increase of 109.4 $km^2$. In contrast, the development of reservoir-based WPV proceeded more slowly. Its expansion was limited between 2015 and 2019 (14.9 $km^2$), and following the introduction of policy restrictions in 2019, reservoir-based WPV installations declined sharply, with the total area remaining below 20 $km^2$. These trends underscore the growing dominance of lakes as preferred sites for WPV deployment, while reservoirs have become increasingly constrained due to operational sensitivities, fluctuating water levels, and tightening environmental regulations (General Office of MWR, 2020).

The impact of WPV systems on water bodies is multifaceted, influencing various physical properties and ecological dynamics, with the extent of WPV coverage exerting differential effects based on water body characteristics (Exley *et al.*, 2021). By integrating WPV distribution data with surface water datasets, WPV coverage was calculated for 385 water bodies across the study area (Figs. 11a, b). Coverage rates varied substantially among different size classes. In smaller water bodies (0–4 $km^2$), WPV coverage exhibited high variability, ranging from 0% to 100%. However, as water body size increased, WPV coverage declined sharply, falling below 50% in medium-sized water bodies and below 10% in large ones (>100 $km^2$). Most reservoirs covered by WPV installations are relatively small (< 4 $km^2$), and their overall WPV coverage is slightly lower than that of lakes of comparable size.

https://doi.org/10.5194/essd-2025-695
Preprint. Discussion started: 20 January 2026




### 3.4 WPV Spatial Clustering and Driving Factors

At the regional scale (Fig. 12a), WPV projects exhibit a clear pattern of localized clustering across the study area. These projects are primarily distributed along major rivers and lakes, with project sizes varying considerably, from less than 0.1 $km^2$ to over 3 $km^2$. Notably, several large, high-density clusters are observed in parts of Jiangsu and Anhui provinces (Fig. 12b-12d).

This spatial aggregation is shaped by a combination of natural and socio-economic factors. Natural conditions provide fundamental support for WPV deployment, with large water bodies having minimal fluctuations in water level and stable water quality being particularly suitable (Woolway *et al.*, 2024). For example, Sanlihe Reservoir (Fig. 12e), Gaoyou Lake (Fig. 12f), and Xizi Lake (Fig. 12g) possess stable, expansive water surfaces and favorable hydrological conditions, supporting extensive WPV arrays. Grid accessibility is another key driver influencing the spatial distribution of WPV systems (Essak and Ghosh, 2022). In both Gaoyou Lake and Xizi Lake, WPV installations are located near urban settlements and existing power infrastructure, which facilitates grid connection and reduces energy transmission losses and associated costs. This locational advantage has made such water bodies prime targets for large-scale WPV deployment.

## 4 Discussion

### 4.1 Major Findings and Contributions

This study constructs a high-precision, decade-long (2015–2024) WPV dataset for the YRD region, thereby significantly advancing remote sensing-based WPV mapping. We specifically address key limitations in existing time-series mapping approaches, namely the constraints of optical imagery (e.g., cloud cover and water surface reflection) and the substantial error accumulation in long-term mapping (e.g., per-period accuracy of ~0.96 may degrade to ~0.67 over ten years). Our robust solution—fusing Sentinel-1 SAR data with multi-temporal Sentinel-2 imagery—effectively leverages SAR's all-weather imaging capability and the strong backscatter signals uniquely associated with the metallic structure of WPV panels, thereby significantly enhancing single-period mapping accuracy and reducing misclassification. In

https://doi.org/10.5194/essd-2025-695
Preprint. Discussion started: 20 January 2026




addition, through probabilistic filtering and meticulous manual verification using high-resolution Google Earth imagery over potential WPV regions, we achieved unprecedented accuracy and temporal consistency for this long-term dataset.

Based on this reliable dataset, we conducted the first systematic and fine-scale decadal analysis of the spatial-temporal distribution and growth trends of WPV in the YRD. We revealed that the total WPV area expanded rapidly from 17.4 $km^2$ in 2015 to 145.4 $km^2$ in 2024, along with a shift in the leading province of development from Jiangsu to Anhui. The results also detail the diverse growth trajectories of large-, medium-, and small-scale WPV projects, demonstrating an evolution from localized concentration to broader regional deployment.

### 4.2 Implications and Potential Applications

This high-precision, decade-long WPV dataset constructed in this study holds significant theoretical and practical value. It strengthens the scientific foundation for WPV deployment, improves the accuracy of environmental impact assessments, and informs more effective policy-making. A primary contribution of the dataset lies in its utility for WPV energy planning and spatial optimization. By quantifying the surface coverage and spatial distribution of WPV installations, and distinguishing their suitability across various water body types (e.g., high-coverage potential under “fishing-solar complementarity” schemes), the dataset enables the identification of optimal deployment zones. This facilitates a balance between rapid WPV expansion and aquatic ecosystem protection, enhancing the efficiency of resource allocation and supporting data-driven site selection and planning (Bai *et al.*, 2024; Château *et al.*, 2019).

In addition, the dataset provides a reliable basis for evaluating the environmental impacts of WPV systems. It supports the assessment of both physical and biological effects on water bodies, including alterations in evaporation rates, thermal dynamics, and impacts on aquatic ecosystems such as algal photosynthesis. This is particularly valuable in identifying potential ecological risks associated with high-coverage installations in small water bodies, thereby promoting more ecologically responsible deployment strategies (Sahu *et al.*, 2016; Armstrong

https://doi.org/10.5194/essd-2025-695
Preprint. Discussion started: 20 January 2026


*et al.*, 2020; Nobre *et al.*, 2023; Ma and Liu, 2022). Furthermore, the dataset enhances the effectiveness of field validation efforts. By addressing limitations of outdated and spatially sparse datasets, it facilitates the targeted selection of representative WPV sites for in-situ investigation, significantly improving the efficiency and accuracy of ground-truthing and data collection.

### 4.3 Limitations and Future Research

Despite constructing a high-precision dataset, this study has several limitations. First, uncertainties in the underlying waterbody datasets remain a challenge; small water bodies (e.g., ponds) may be omitted, while imprecise boundaries and spectral confusion with nearby buildings or bare soil can cause both omissions and misclassifications at water edges (Valerio *et al.*, 2024; Wang *et al.*, 2022). Second, the diversity in WPV installation methods and structural designs introduces variations in spectral and textural characteristics, posing challenges for consistent extraction (Shi *et al.*, 2023). Finally, the area threshold applied during post-processing to eliminate noise likely leads to an underestimation of the total WPV area, particularly by excluding small-scale systems on rural ponds or aquaculture facilities (Iqra *et al.*, 2024).

In light of these limitations, future research can focus on three key directions. Methodologically, the integration of deep learning methods (e.g., U-Net, DeepLabV3+) holds promise for enhancing accuracy, particularly in delineating complex boundaries and detecting morphologically diverse or small-scale targets (Chen *et al.*, 2018; Ronneberger *et al.*, 2015). Spatially, expanding the study to national or global scales would reveal macro-level deployment trends driven by policy and market dynamics, offering valuable guidance for macro-level energy planning. Thematically, future work should place greater emphasis on evaluating the ecological impacts of WPY systems by integrating remote sensing retrievals with in-situ monitoring data, thereby promoting a coordinated approach to renewable energy development and ecosystem conservation.

https://doi.org/10.5194/essd-2025-695
Preprint. Discussion started: 20 January 2026




448

449 **5 Conclusion**

450 This study precisely mapped the spatiotemporal distribution of Water-surface photovoltaic
451 (WPV) systems in China's Yangtze River Delta from 2015 to 2024. Using a robust framework
452 that integrated multi-temporal Sentinel-1 SAR and Sentinel-2 optical imagery with Random
453 Forest classification, refined by post-processing and manual verification, we generated a high-
454 resolution, decade-long dataset that overcomes optical imagery limitations and cumulative
455 errors in long-term monitoring. Our findings reveal WPV's significant expansion (17.4 $km^2$ in
456 2015 to 145.4 $km^2$ in 2024), with deployment shifting towards Anhui. Most projects are now
457 small- to medium-scale, primarily on lakes, exhibiting clear spatial clustering influenced by
458 water conditions and grid access. This comprehensive WPV mapping serves as a critical data
459 source for assessing development potential, guiding renewable energy planning, and evaluating
460 ecological impacts. Its generalizable methodology offers a strong foundation for broader WPV
461 monitoring and future research integrating advanced remote sensing and ecological analysis.

462

463

https://doi.org/10.5194/essd-2025-695
Preprint. Discussion started: 20 January 2026




## Acknowledgments

This study was supported by the National Natural Science Foundation of China - United Nations Environment Programme (NSFC-UNEP, no. 42361144001), National Natural Science Foundation of China (no. 42071022), Shenzhen Science and Technology Project for Sustainable Development in Special Innovation (no. KCXFZ20230731093403008), Guangdong Basic and Applied Basic Research Foundation (no. 2022A1515240070), the Shenzhen Key Laboratory of Precision Measurement and Early Warning Technology for Urban Environmental Health Risks (no. ZDSYS20220606100604008) and the start-up and high-level special funds provided by the Southern University of Science and Technology (no. 29/Y01296602; 29/Y01296122; 29/Y01296222; G030290001). This work is supported with the High Performance Computing Centers (Taiyi) at SUSTech.

## Data availability

The Yangtze River Delta Water-Surface Photovoltaics Dataset (2015–2024) is available at https://doi.org/10.5281/zenodo.17484488 (Yan et al., 2025).

## CRediT authorship contribution statement

Yue Yan contributed to conceptualization, data curation, formal analysis, visualization, and writing – original draft. Zhenzhong Zeng was responsible for funding acquisition, project administration, supervision, and writing – review & editing, serving as corresponding author. Xin Jiang provided supervision, methodology guidance, and writing – review & editing. All other authors contributed to investigation, validation, and writing – review & editing.

## Declaration of competing interest

The authors declare that they have no known competing financial interests or personal relationships that could have appeared to influence the work reported in this paper.

https://doi.org/10.5194/essd-2025-695
Preprint. Discussion started: 20 January 2026




## References

Armstrong, A., Page, T., Thackeray, S. J., Hernandez, R. R., and Jones, I. D.: Integrating environmental understanding into freshwater floatovoltaic deployment using an effects hierarchy and decision trees, Environ. Res. Lett., 15, 114055, doi:10.1088/1748-9326/abbf7b, 2020.

Bai, B., Xiong, S., Ma, X., and Liao, X.: Assessment of floating solar photovoltaic potential in China, Renew. Energy, 220, 119572, doi:10.1016/j.renene.2023.119572, 2024.

Belgiu, M., and Drăguţ, L.: Random forest in remote sensing: A review of applications and future directions, ISPRS J. Photogramm. Remote Sens., 114, 24–31, doi:10.1016/j.isprsjprs.2016.01.011, 2016.

Bogdanov, D. et al.: Low-cost renewable electricity as the key driver of the global energy transition towards sustainability, Energy, 227, 120467, doi:10.1016/j.energy.2021.120467, 2021.

Robinson, C., Ortiz, A., Kim, A., Dodhia, R., Zolli, A., Nagaraju, S. K., Oakleaf, J., Kiesecker, J., and Ferres, J. M. L.: Global Renewables Watch: A Temporal Dataset of Solar and Wind Energy Derived from Satellite Imagery, arXiv, doi:10.48550/arXiv.2503.14860, 2025.

Capellán-Pérez, I., De Castro, C., and Arto, I.: Assessing vulnerabilities and limits in the transition to renewable energies: Land requirements under 100% solar energy scenarios, Renew. Sustain. Energy Rev., 77, 760–782, doi:10.1016/j.rser.2017.03.137, 2017.

Château, P.-A., Wunderlich, R. F., Wang, T.-W., Lai, H.-T., Chen, C.-C., and Chang, F.-J.: Mathematical modeling suggests high potential for the deployment of floating photovoltaic on fish ponds, Sci. Total Environ., 687, 654–666, doi:10.1016/j.scitotenv.2019.05.420, 2019.

Chen, L.-C., Zhu, Y., Papandreou, G., Schroff, F., and Adam, H.: Encoder-Decoder with Atrous Separable Convolution for Semantic Image Segmentation, Comput. Vis. ECCV, 2018, 833–851, doi:10.1007/978-3-030-01234-2_49, 2018.

Chen, Y., Zhou, J., Ge, Y., and Dong, J.: Uncovering the rapid expansion of photovoltaic power

https://doi.org/10.5194/essd-2025-695
Preprint. Discussion started: 20 January 2026




515 plants in China from 2010 to 2022 using satellite data and deep learning, Remote Sens.
516 Environ., 305, 114100, doi:10.1016/j.rse.2024.114100, 2024.
517 Chen, Z., Kang, Y., Sun, Z., Wu, F., and Zhang, Q.: Extraction of photovoltaic plants using
518 machine learning methods: A case study of the pilot energy city of Golmud, China,
519 Remote Sens., 14, 12697, doi:10.3390/rs14112697, 2022.
520 Essak, L., and Ghosh, A.: Floating photovoltaics: A review, Clean Technol., 4, 466–493,
521 doi:10.3390/cleantechnol4030046, 2022.
522 Exley, G., Armstrong, A., Page, T., and Jones, I. D.: Floating photovoltaics could mitigate
523 climate change impacts on water body temperature and stratification, Sol. Energy, 219,
524 24–33, doi:10.1016/j.solener.2021.01.076, 2021.
525 Feng, Q., Niu, B., Ren, Y., Su, S., Wang, J., Shi, H., Yang, J., and Han, M.: A 10-m national-
526 scale map of ground-mounted photovoltaic power stations in China of 2020, Sci. Data,
527 11, 198, doi:10.1038/s41597-024-02994-x, 2024.
528 Forester, E., Levin, M. O., Thorne, J. H., Armstrong, A., Pasquale, G., Vincenza Di Blasi, M.
529 L., Scott, T. A., and Hernandez, R. R.: Siting considerations for floating solar
530 photovoltaic energy: A systematic review, Renew. Sustain. Energy Rev., 211, 115360,
531 doi:10.1016/j.rser.2025.115360, 2025.
532 General Office of the Ministry of Water Resources of the People's Republic of China: Notice
533 on Further Strengthening the Management of Construction Projects within River and
534 Lake Management Scope, Ministry of Water Resources, Beijing, 2020.
535 Global Energy Review 2025: Int. Energy Agency, https://www.iea.org/reports/global-energy-
536 review-2025, 2025.
537 Gorelick, N., Hancher, M., Dixon, M., Ilyushchenko, S., Thau, D., and Moore, R.: Google Earth
538 Engine: Planetary-scale geospatial analysis for everyone, Remote Sens. Environ., 202,
539 18–27, doi:10.1016/j.rse.2017.06.031, 2017.
540 Haralick, R. M., Shanmugam, K., and Dinstein, I.: Textural features for image classification,
541 IEEE Trans. Syst. Man Cybern., SMC-3, 610–621, doi:10.1109/TSMC.1973.4309314,
542 1973.
543 Hirayama, H., Sharma, R. C., Tomita, M., and Hara, K.: Evaluating multiple classifier system

https://doi.org/10.5194/essd-2025-695
Preprint. Discussion started: 20 January 2026




for the reduction of salt-and-pepper noise in the classification of very-high-resolution satellite images, Int. J. Remote Sens., 40, 2542–2557, doi:10.1080/01431161.2018.1528400, 2019.

Iqra, G., Giri, K. J., and Javed, M.: Small object detection in diverse application landscapes: A survey, Multimed. Tools Appl., 83, 88645–88680, doi:10.1007/s11042-024-18866-w, 2024.

Jin, Y. et al.: Energy production and water savings from floating solar photovoltaics on global reservoirs, Nat. Sustain., 6, 865–874, doi:10.1038/s41893-023-01089-6, 2023.

Kruitwagen, L., Story, K. T., Friedrich, J., Byers, L., Skillman, S., and Hepburn, C.: A global inventory of photovoltaic solar energy generating units, Nature, 598, 604–610, doi:10.1038/s41586-021-03957-7, 2021.

Lehner, B., Liermann, C. R., Revenga, C., Vörösmarty, C., Fekete, B., Crouzet, P., Döll, P., Endejan, M., Frenken, K., Magome, J., Nilsson, C., Robertson, J. C., Rödel, R., Sindorf, N., and Wisser, D.: High-resolution mapping of the world's reservoirs and dams for sustainable river-flow management, Front. Ecol. Environ., 9, 494–502, doi:10.1890/100125, 2011.

Ma, C., and Liu, Z.: Water-surface photovoltaics: Performance, utilization, and interactions with water eco-environment, Renew. Sustain. Energy Rev., 167, 112823, doi:10.1016/j.rser.2022.112823, 2022.

Messager, M. L., Lehner, B., Grill, G., Nedeva, I., and Schmitt, O.: Estimating the volume and age of water stored in global lakes using a geo-statistical approach, Nat. Commun., 7, 1–11, doi:10.1038/ncomms13603, 2016.

Mulligan, M., van Soesbergen, A., and Sáenz, L.: GOODD, a global dataset of more than 38,000 georeferenced dams, Sci. Data, 7, 1–8, doi:10.1038/s41597-020-0362-5, 2020.

Nobre, R., Boulêtreau, S., Colas, F., Azemar, F., Tudesque, L., Parthuisot, N., Favriou, P., and Cucherousset, J.: Potential ecological impacts of floating photovoltaics on lake biodiversity and ecosystem functioning, Renew. Sustain. Energy Rev., 188, 113852, doi:10.1016/j.rser.2023.113852, 2023.

Ortiz, A., Negandhi, D., Mysorekar, S. R., Nagaraju, S. K., Kiesecker, J., Robinson, C., Bhatia,

https://doi.org/10.5194/essd-2025-695
Preprint. Discussion started: 20 January 2026




P., Khurana, A., Wang, J., Oviedo, F., and Ferres, J. L.: An Artificial Intelligence Dataset for Solar Energy Locations in India, Sci. Data, 9, 497, doi:10.1038/s41597-022-01499-9, 2022.

Pouran, H. M., Padilha Campos Lopes, M., Nogueira, T., Alves Castelo Branco, D., and Sheng, Y.: Environmental and technical impacts of floating photovoltaic plants as an emerging clean energy technology, iScience, 25, 105253, doi:10.1016/j.isci.2022.105253, 2022.

Ronneberger, O., Fischer, P., and Brox, T.: U-Net: Convolutional Networks for Biomedical Image Segmentation, arXiv preprint, arXiv:1505.04597, doi:10.48550/arXiv.1505.04597, 2015.

Sahu, A., Yadav, N., and Sudhakar, K.: Floating photovoltaic power plant: A review, Renew. Sustain. Energy Rev., 66, 815–824, doi:10.1016/j.rser.2016.08.051, 2016.

Shi, W., Yan, C., Ren, Z., Yuan, Z., Liu, Y., Zheng, S., Li, X., and Han, X.: Review on the development of marine floating photovoltaic systems, Ocean Eng., 286, 115560, doi:10.1016/j.oceaneng.2023.115560, 2023.

Valerio, F., Godinho, S., Ferraz, G., Pita, R., Gameiro, J., Silva, B., Marques, A. T., and Silva, J. P.: Multi-temporal remote sensing of inland surface waters: A fusion of Sentinel-1 & Sentinel-2 data applied to small seasonal ponds in semiarid environments, Int. J. Appl. Earth Obs. Geoinf., 135, 104283, doi:10.1016/j.jag.2024.104283, 2024.

van de Ven, D.-J., Capellán-Pérez, I., Arto, I., Cazcarro, I., De Castro, C., Patel, P., and Gonzalez-Eguino, M.: The potential land requirements and related land use change emissions of solar energy, Sci. Rep., 11, 2907, doi:10.1038/s41598-021-82042-5, 2021.

Wang, J., Walter, B. A., Yao, F., Song, C., Ding, M., Maroof, A. S., Zhu, J., Fan, C., McAlister, J. M., Sikder, S., Sheng, Y., Allen, G. H., Crétaux, J.-F., and Wada, Y.: GeoDAR: Georeferenced global dams and reservoirs dataset for bridging attributes and geolocations, Earth Syst. Sci. Data, 14, 1869–1899, doi:10.5194/essd-14-1869-2022, 2022.

Wang, L., Bie, W., Li, H., Liao, T., Ding, X., Wu, G., and Fei, T.: Small water body detection and water quality variations with changing human activity intensity in Wuhan, Remote Sens., 14, 200, doi:10.3390/rs14010200, 2022.

https://doi.org/10.5194/essd-2025-695
Preprint. Discussion started: 20 January 2026




602 Wei, S., Chen, Y., and Zeng, Z.: An unexpectedly large proportion of photovoltaic facilities
603 installed on cropland, Innov. Energy, 2, 100070–100073, doi:10.59717/j.xinn-
604 energy.2024.100070, 2025.
605 Woolway, R. I., Zhao, G., Rocha, S. M. G., Thackeray, S. J., and Armstrong, A.:
606 Decarbonization potential of floating solar photovoltaics on lakes worldwide, Nat.
607 Water, 2, 566–576, doi:10.1038/s44221-024-00251-4, 2024.
608 Xia, Z., Li, Y., Guo, S., Chen, R., Zhang, W., Zhang, P., and Du, P.: Mapping global water-
609 surface photovoltaics with satellite images, Renew. Sustain. Energy Rev., 187, 113760,
610 doi:10.1016/j.rser.2023.113760, 2023.
611 Xia, Z., Li, Y., Guo, X., and Chen, R.: High-resolution mapping of water photovoltaic
612 development in China through satellite imagery, Int. J. Appl. Earth Obs. Geoinf., 107,
613 102707, doi:10.1016/j.jag.2022.102707, 2022.
614 Xu, C., Xie, D., Gu, C., Zhao, P., Wang, X., and Wang, Y.: Sustainable development pathways
615 for energies in Yangtze River Delta urban agglomeration, Sci. Rep., 13, 18135,
616 doi:10.1038/s41598-023-44727-x, 2023.
617 Yan, Y., Jiang, X., Wei, S., Jin, Y., Zou, X., Liu, J., Cai, Y., Ye, J., Guo, Z., and Zeng, Z.:
618 Yangtze River Delta Water-Surface Photovoltaics Dataset (2015–2024), Zenodo [data
619 set], https://doi.org/10.5281/zenodo.17484488, 2025.
620 Zhang, H., Tian, P., Zhong, J., Liu, Y., and Li, J.: Mapping photovoltaic panels in coastal China
621 using Sentinel-1 and Sentinel-2 images and Google Earth Engine, Remote Sens., 15,
622 3712, doi:10.3390/rs15153712, 2023.
623 Zhang, X., Xu, M., Wang, S., Huang, Y., and Xie, Z.: Mapping photovoltaic power plants in
624 China using Landsat, random forest, and Google Earth Engine, Earth Syst. Sci. Data,
625 14, 3743–3755, doi:10.5194/essd-14-3743-2022, 2022.
626 Zhang, X., Zeraatpisheh, M., Rahman, M. M., Wang, S., and Xu, M.: Texture is important in
627 improving the accuracy of mapping photovoltaic power plants: A case study of Ningxia
628 Autonomous Region, China, Remote Sens., 13, 3909, doi:10.3390/rs13193909, 2021.
629

https://doi.org/10.5194/essd-2025-695
Preprint. Discussion started: 20 January 2026


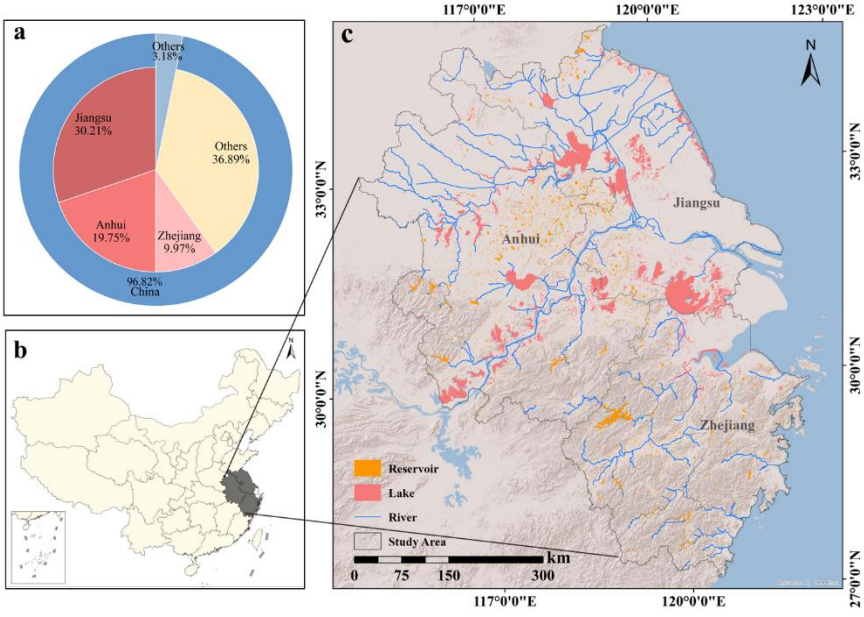


**Figure 1. WPV distribution and overview of the study area.** a: Proportions of WPV area in the study area relative to China, with specific contributions from Jiangsu, Anhui, and Zhejiang provinces; b: Location of the study area within China; c: Spatial distribution of reservoirs, lakes, and rivers in the study area. Basemap: © Esri, TomTom, FAO, NOAA, USGS. Powered by Esri.

https://doi.org/10.5194/essd-2025-695
Preprint. Discussion started: 20 January 2026


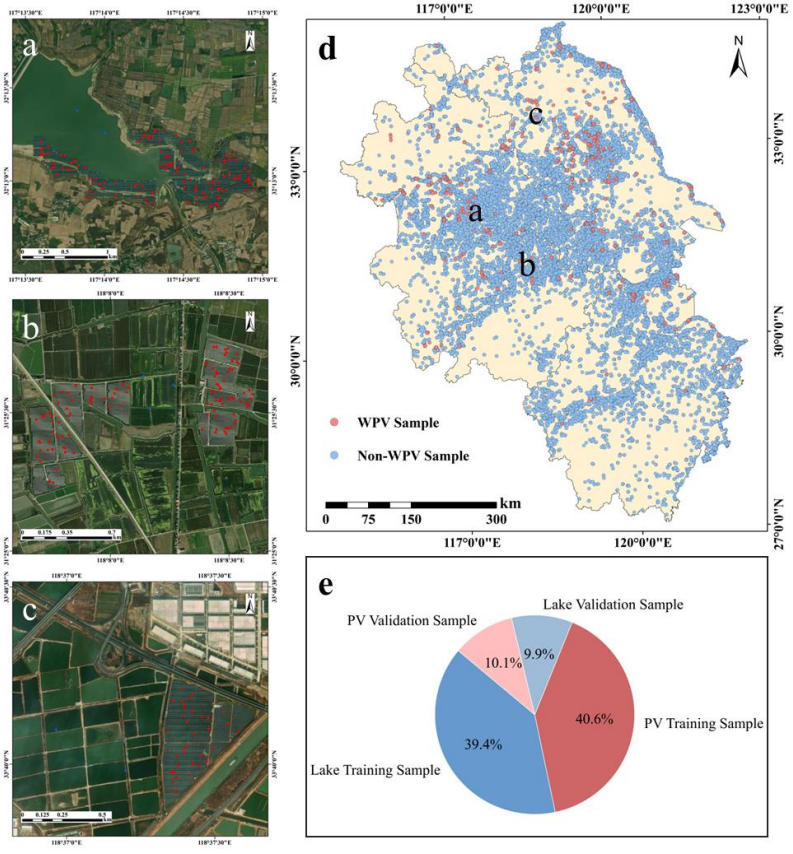


**Figure 2. Distribution and examples of samples.** a: Spatial distribution of WPV and Non-WPV samples across the study area; b: Proportions of different sample categories; c–e: Examples of typical sample regions, where red points indicate WPV samples and blue points indicate Non-WPV samples. Basemap: © Esri, DigitalGlobe, GeoEye, i-cubed, USDA FSA, USGS, AEX, Getmapping, Aerogrid, IGN, IGP, swisstopo, and the GIS User Community. Powered by Esri.

https://doi.org/10.5194/essd-2025-695
Preprint. Discussion started: 20 January 2026


Open Access Earth System Science Data Discussions

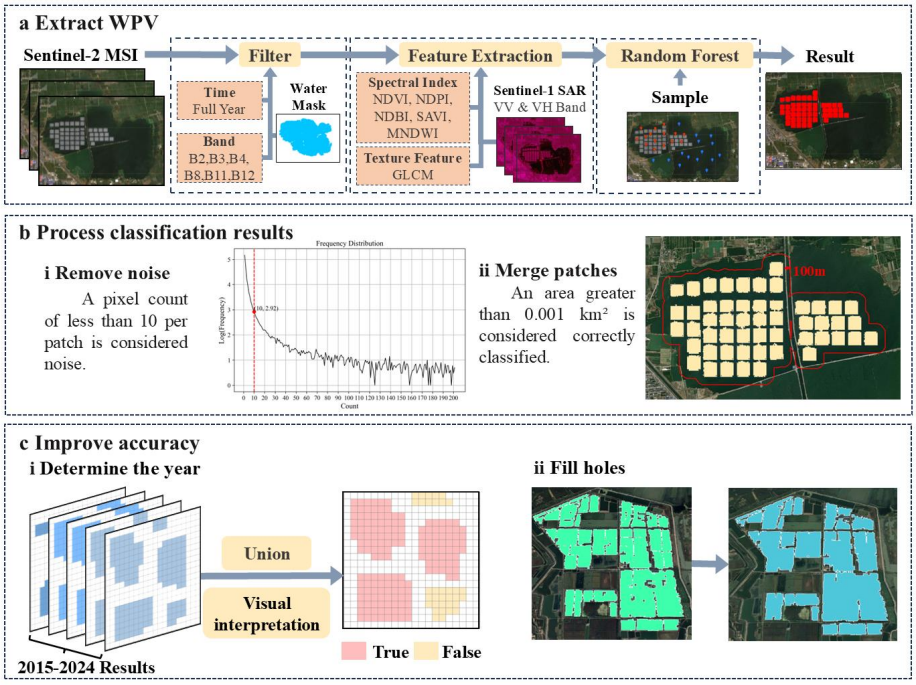


**Figure 3. Flowchart of the method for extracting WPV from satellite imagery.** a: WPV extraction process based on Sentinel-2 MSI and Sentinel-1 SAR data, including water masking, feature extraction (spectral indices, texture features, SAR bands), and classification using a Random Forest model; b: Post-processing of classification results: i: removing noise patches smaller than 10 pixels, and ii: merging patches within 200 meters of each other and retaining those with an area greater than 0.0001 $km^2$; c: Accuracy improvement strategies: i: determining the year of installation using annual union and visual interpretation, and ii: filling small holes in classified patches. The final dataset covers the period from 2015 to 2024. Basemap: © Esri, DigitalGlobe, GeoEye, i-cubed, USDA FSA, USGS, AEX, Getmapping, Aerogrid, IGN, IGP, swisstopo, and the GIS User Community. Powered by Esri.

https://doi.org/10.5194/essd-2025-695
Preprint. Discussion started: 20 January 2026


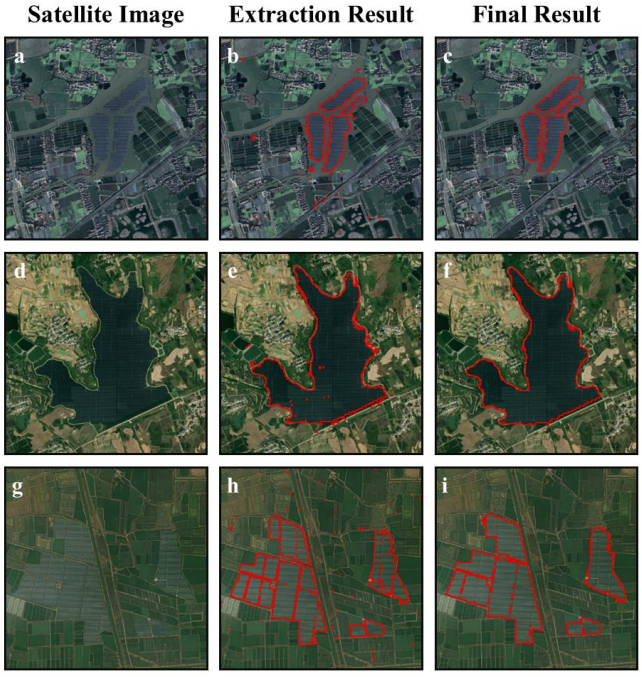


**Figure 4. Examples of WPV extraction results.** Panels a–c, d–f, and g–i show three representative areas. a, d, g: The satellite images; b, e, h: The initial extraction results; c, f, i: The final results after manual correction. Red outlines indicate the boundaries of WPV areas. The three areas are located at a–c: 30°51′40.54″N, 120°44′30.47″E; d–f: 32°06′03.69″N, 117°33′00.10″E; g–i: 32°58′06.10″N, 119°37′09.47″E. Basemap: © Esri, DigitalGlobe, GeoEye, i-cubed, USDA FSA, USGS, AEX, Getmapping, Aerogrid, IGN, IGP, swisstopo, and the GIS User Community. Powered by Esri.

https://doi.org/10.5194/essd-2025-695
Preprint. Discussion started: 20 January 2026


Open Access Earth System Science Data Discussions

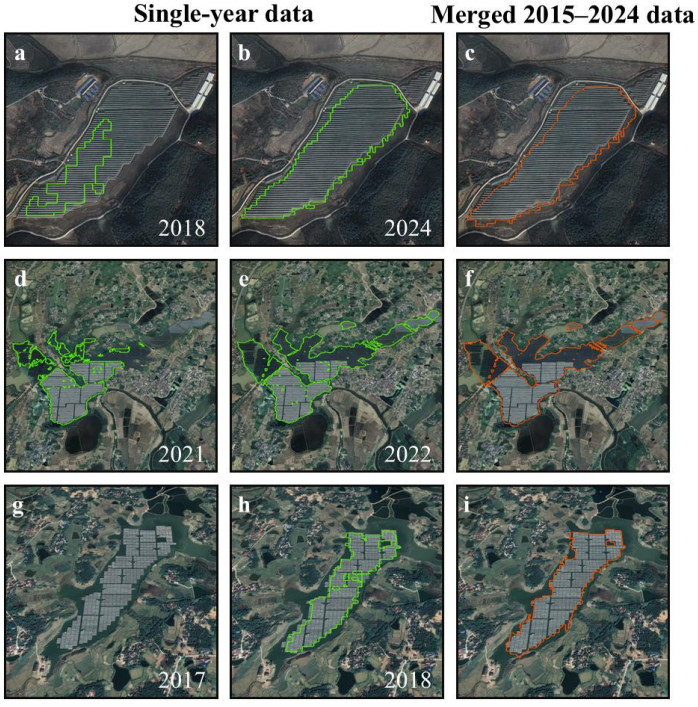


665

666 **Figure 5. Comparison between single-year and merged multi-year data for WPV**
667 **extraction on lakes.** Panels a–c, d–f, and g–i are three representative areas. a, d, g, and b, e, h:
668 WPV extraction results from single-year images of different years, outlined in green; c, f, i: The
669 extraction results based on the merged 2015–2024 dataset, outlined in orange. The three areas
670 are located at a–c: 30°22′19.59″N, 116°21′50.00″E; d–f: 30°36′26.69″N, 117°17′45.92″E; and
671 g–i: 30°44′55.34″N, 116°57′05.93″E. Basemap: © Esri, DigitalGlobe, GeoEye, i-cubed, USDA
672 FSA, USGS, AEX, Getmapping, Aerogrid, IGN, IGP, swisstopo, and the GIS User Community.
673 Powered by Esri.

674

https://doi.org/10.5194/essd-2025-695
Preprint. Discussion started: 20 January 2026




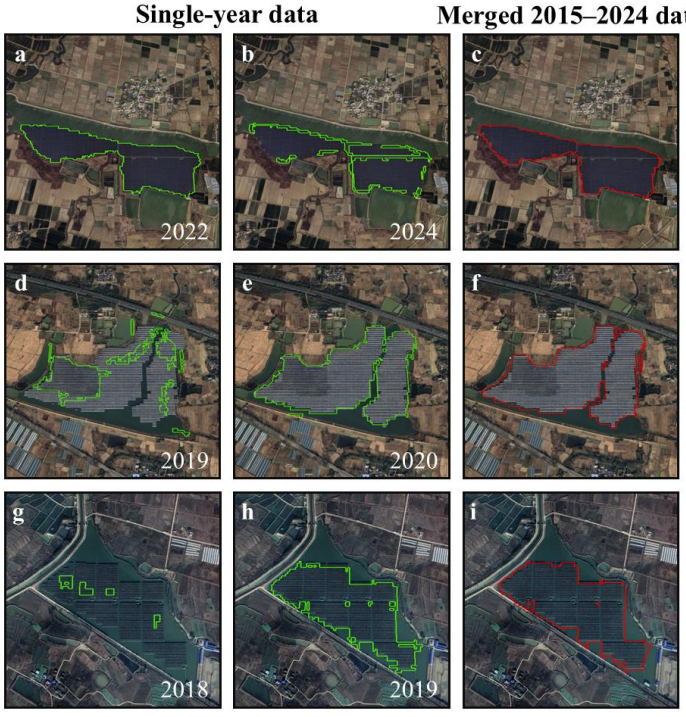


675

676 **Figure 6. Comparison between single-year and merged multi-year data for WPV**
677 **extraction on reservoirs.** Panels a–c, d–f, and g–i are three representative areas. a, d, g, and b,
678 e, h: WPV extraction results from single-year images of different years, outlined in green; c, f,
679 i: The extraction results based on the merged 2015–2024 dataset, outlined in red. The three areas
680 are located at a–c: 32°43′54.10″N, 117°41′35.43″E; d–f: 32°33′04.04″N, 116°55′38.40″E; and
681 g–i: 32°11′46.56″N, 117°02′51.31″E. Basemap: © Esri, DigitalGlobe, GeoEye, i-cubed, USDA
682 FSA, USGS, AEX, Getmapping, Aerogrid, IGN, IGP, swisstopo, and the GIS User Community.
683 Powered by Esri.

684

https://doi.org/10.5194/essd-2025-695
Preprint. Discussion started: 20 January 2026


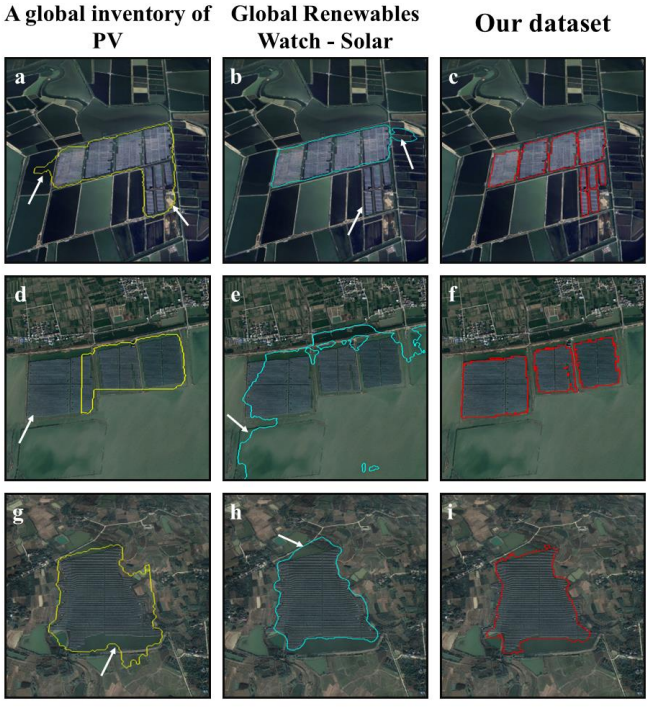


685

686 **Figure 7. Comparison of our FPV extraction results with two global PV datasets**
687 **(Kruitwagen *et al.*, 2021; Robinson *et al.*, 2025): examples of incomplete and incorrect**
688 **identification.** Panels a–c, d–f, and g–i are three representative areas. a, d, g: A global inventory
689 of PV Kruitwagen *et al.*, 2021, outlined in yellow; b, e, h: Global Renewables Watch, 2023,
690 outlined in blue; c, f, i: Our extraction results, outlined in red. The three areas are located at a–
691 c: 31°07′51.26″N, 119°02′42.41″E; d–f: 32°36′34.53″N, 116°34′24.75″E; g–i: 31°35′19.28″N,
692 117°06′36.42″E. Basemap: © Esri, DigitalGlobe, GeoEye, i-cubed, USDA FSA, USGS, AEX,
693 Getmapping, Aerogrid, IGN, IGP, swisstopo, and the GIS User Community. Powered by Esri.

694

https://doi.org/10.5194/essd-2025-695
Preprint. Discussion started: 20 January 2026


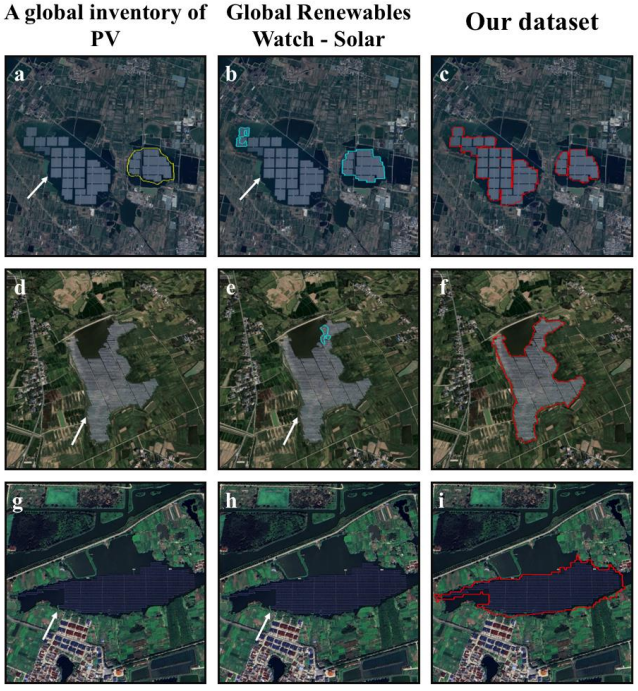


**Figure 8. Comparison of our FPV extraction results with two global PV datasets (Kruitwagen *et al.*, 2021; Robinson *et al.*, 2025): examples of undetected FPV installations.** Panels a–c, d–f, and g–i are three representative areas. a, d, g: A global inventory of PV Kruitwagen *et al.*, 2021, outlined in yellow; b, e, h: Global Renewables Watch, 2023, outlined in blue; c, f, i: Our extraction results, outlined in red. The three representative lake areas are located at a–c: 32°49′16.10″N, 116°49′57.69″E; d–f: 32°20′36.04″N, 117°21′11.29″E; g–i: 32°34′46.60″N, 119°58′03.91″E. Basemap: © Esri, DigitalGlobe, GeoEye, i-cubed, USDA FSA, USGS, AEX, Getmapping, Aerogrid, IGN, IGP, swisstopo, and the GIS User Community. Powered by Esri.

https://doi.org/10.5194/essd-2025-695
Preprint. Discussion started: 20 January 2026


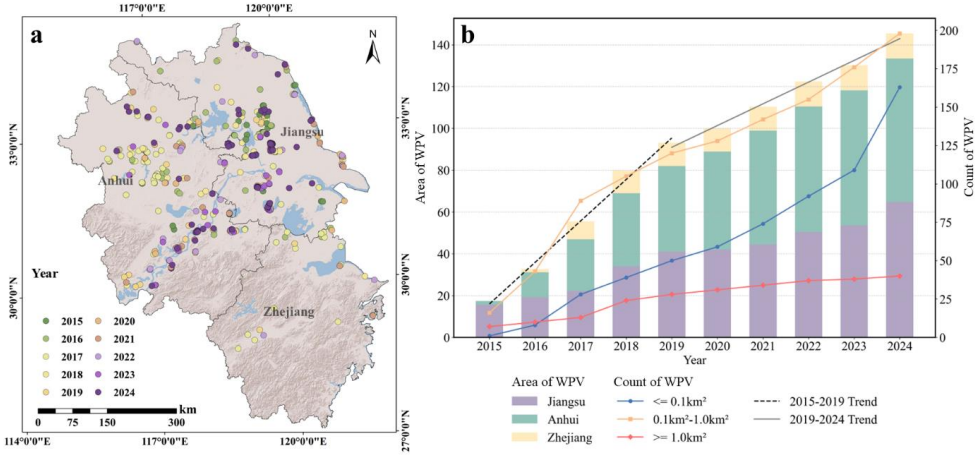


**Figure 9. Spatiotemporal evolution of WPV installations from 2015 to 2024.** a: Spatial distribution of WPV installations from 2015 to 2024 in Jiangsu, Anhui, and Zhejiang provinces, colored by year; b: Temporal evolution of WPV area and count during 2015–2024, where the stacked bars represent WPV area contributions from each province, and the lines indicate the count of WPV installations classified by size (≤0.1 $km^2$, 0.1–1.0 $km^2$, ≥1.0 $km^2$). Dashed and solid lines represent the fitting trends for 2015–2019 and 2019–2024, respectively. Basemap: © Esri, TomTom, FAO, NOAA, USGS. Powered by Esri.

https://doi.org/10.5194/essd-2025-695
Preprint. Discussion started: 20 January 2026


Open Access Earth System Science Data Discussions

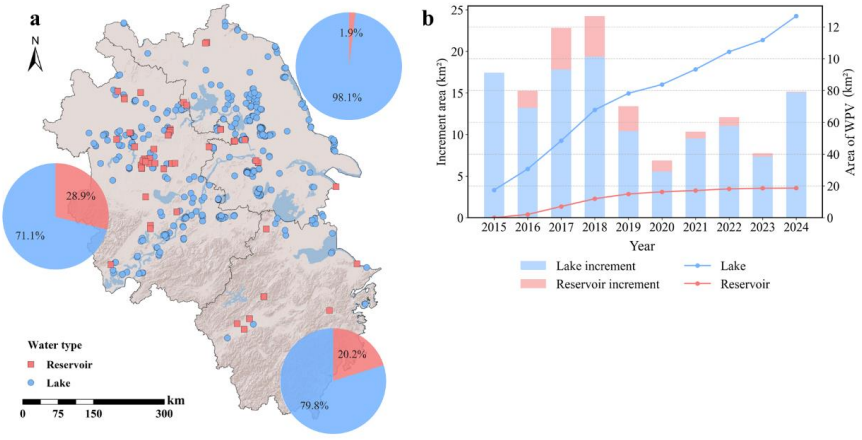


**Figure 10. Spatial and temporal characteristics of WPV systems on different water body types in the Yangtze River Delta.** a: Spatial distribution of WPVs on lakes (blue circles) and reservoirs (red squares), with pie charts indicating the proportion of WPV area on each water type in Jiangsu (top right), Zhejiang (bottom right), and Anhui (left); b: Annual WPV area increments on lakes and reservoirs from 2015 to 2024. Bars represent yearly increments, and lines represent cumulative area on each water type. Basemap: © Esri, TomTom, FAO, NOAA, USGS. Powered by Esri.

https://doi.org/10.5194/essd-2025-695
Preprint. Discussion started: 20 January 2026


Open Access Earth System Science Data Discussions

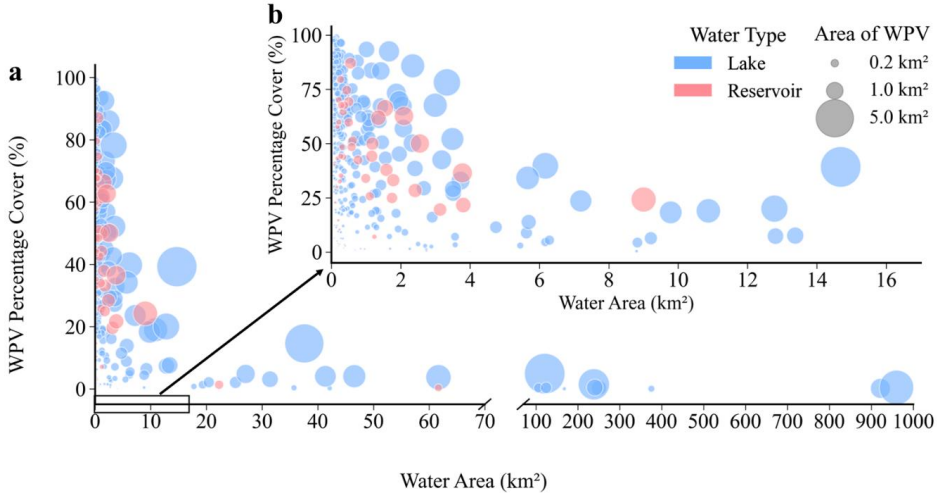


726

727 **Figure 11. Relationship between water area and WPV percentage cover across lakes and**
728 **reservoirs.** a: Distribution of WPV percentage cover (%) against water body area ($km^2$), with
729 circle size representing the WPV area; b: Enlarged view of the 0–10 $km^2$ water area range to
730 highlight clustering patterns. Blue and red colors represent lakes and reservoirs, respectively,
731 and circle size denotes WPV area.

732

https://doi.org/10.5194/essd-2025-695
Preprint. Discussion started: 20 January 2026


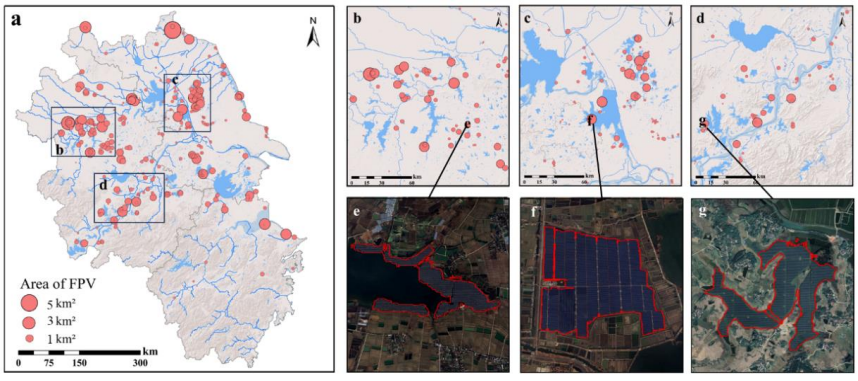


733

734 **Figure 12. Spatial Clustering and Local Layouts of WPV Installations.** a: Distribution of
735 WPV systems across Jiangsu, Anhui, and Zhejiang provinces. The size of the red circles
736 represents the area of each WPV system; b–d: Enlarged views of typical clustered regions
737 highlighted in a; e–g: Satellite images showing detailed layouts of selected WPV systems
738 corresponding to the locations indicated in b–d, with WPV boundaries outlined in red. Basemap:
739 © Esri, TomTom, FAO, NOAA, USGS, DigitalGlobe, GeoEye, i-cubed, USDA FSA, AEX,
740 Getmapping, Aerogrid, IGN, IGP, swisstopo, and the GIS User Community. Powered by Esri.

741

https://doi.org/10.5194/essd-2025-695
Preprint. Discussion started: 20 January 2026


Open Access Earth System Science Data Discussions

742 **Table 1. Validation of the accuracy of the classification results.**

| Dataset | A global inventory of PV | Global Renewables Watch | Our dataset |
|---|---|---|---|
| **User Accuracy (%)** | 73.8 | 73.1 | 96.9 |
| **Producer Accuracy (%)** | 65.6 | 64.5 | 97.0 |
| **Overall Accuracy (%)** | 82.5 | 81.8 | 97.5 |
| **Kappa Coefficient** | 0.651 | 0.637 | 0.949 |

743

744

https://doi.org/10.5194/essd-2025-695
Preprint. Discussion started: 20 January 2026




745 **Table 2. The top 5 largest WPV areas in each province.**

| Province | City | Year | Type | Area ($km^2$) | Water Area ($km^2$) | Coordinates |
|---|---|---|---|---|---|---|
| Anhui | Fuyang | 2022 | Lake | 3.53 | 4.21 | 32°48′N, 116°14′E |
| | Huainan | 2017 | Lake | 2.29 | 61.67 | 32°41′N, 117°07′E |
| | Lu'an | 2016 | Lake | 1.97 | 238.35 | 32°08′N, 116°46′E |
| | Chuzhou | 2018 | Lake | 1.95 | 960.42 | 32°48′N, 119°07′E |
| | Anqing | 2021 | Lake | 1.93 | 2.99 | 30°47′N, 117°31′E |
| Jiangsu | Lianyungang | 2024 | Lake | 5.76 | 14.69 | 34°42′N, 119°09′E |
| | Xuzhou | 2022 | Lake | 2.60 | 3.33 | 34°54′N, 116°50′E |
| | Suqian | 2018 | Lake | 2.55 | 37.58 | 33°15′N, 117°57′E |
| | Yangzhou | 2019 | Lake | 2.22 | 121.18 | 33°17′N, 119°41′E |
| | Huaian | 2015 | Lake | 2.12 | 960.42 | 32°56′N, 119°14′E |
| Zhejiang | Ningbo | 2017 | Lake | 2.40 | 6.17 | 30°17′N, 121°06′E |
| | Ningbo | 2018 | Reservoir | 2.18 | 9.00 | 30°01′N, 121°37′E |
| | Jiaxing | 2017 | Lake | 1.35 | 3.18 | 30°56′N, 120°48′E |
| | Huzhou | 2017 | Lake | 0.96 | 3.51 | 30°40′N, 120°08′E |
| | Huzhou | 2017 | Reservoir | 0.60 | 1.59 | 30°49′N, 119°43′E |

746